

1 Abstract

- 2 1. Accurate quantification of soil carbon fluxes is essential to reduce uncertainty in esti-
3 mations of the terrestrial carbon sink. However, these fluxes vary over time and across
4 ecosystem types and so it can be difficult to estimate them accurately across large scales.
5 The flux gradient method estimates soil carbon fluxes using co-located measurements of
6 soil CO₂ concentration, soil temperature, soil moisture, and other soil properties. The
7 National Ecological Observatory Network (NEON) provides such data across 20 ecocli-
8 matic domains spanning the continental U.S., Puerto Rico, Alaska, and Hawai‘i.
- 9 2. We present an R software package (`neonSoilFlux`) that acquires soil environmental data
10 to compute half-hourly soil carbon fluxes for each soil replicate plot at a given terrestrial
11 NEON site. To assess the computed fluxes, we visited six focal NEON sites and measured
12 soil carbon fluxes using a closed-dynamic chamber approach.
- 13 3. Outputs from the `neonSoilFlux` showed agreement with measured fluxes (R^2 between
14 measured and `neonSoilFlux` outputs ranging from 0.12 to 0.77 depending on calculation
15 method used); measured outputs generally fell within the range of calculated uncertain-
16 ties from the gradient method. Calculated fluxes from `neonSoilFlux` aggregated to the
17 daily scale exhibited expected site-specific seasonal patterns.
- 18 4. While the flux gradient method is broadly effective, its accuracy is highly sensitive to
19 site-specific inputs, including the extent to which gap-filling techniques are used to in-
20 terpolate missing sensor data and to estimates of soil diffusivity and moisture content.
21 Future refinement and validation of `neonSoilFlux` outputs can contribute to existing
22 databases of soil carbon flux measurements, providing near real-time estimates of a crit-
23 ical component of the terrestrial carbon cycle.

²⁴ **1.1 Keywords**

²⁵ Soil carbon, carbon dioxide, flux gradient, carbon cycle, field validation, soil respiration, ecosys-
²⁶ tem variability, diffusion

²⁷ **2 Introduction**

²⁸ Soils contain the planet's largest reservoir of terrestrial carbon (Jobbág & Jackson, 2000). A
²⁹ critical component of this reservoir is soil organic matter, the accumulation of which is influ-
³⁰ enced by biotic factors such as above-ground plant inputs (Jackson et al., 2017). These inputs
³¹ in turn are influenced by environmental factors such as growing season length, temperature,
³² and moisture (Desai et al., 2022), which also affect the breakdown of soil organic matter and its
³³ return to the atmosphere. Across heterogeneous terrestrial landscapes, the interplay between
³⁴ these biotic and abiotic factors influence the size of the soil contribution to the terrestrial
³⁵ carbon sink (Friedlingstein et al., 2025). However, the heterogeneity of these processes across
³⁶ diverse ecosystems in the context of rapid environmental change leads to large uncertainty
³⁷ about the magnitude of this sink in the future, and thus there remains a pressing need to
³⁸ quantify changes in soil carbon pools and fluxes across scales.

³⁹ Ecological observation networks such as the United States' National Ecological Observatory
⁴⁰ Network (NEON) and others (e.g. the globally-distributed FLUXNET or the European Inte-
⁴¹ grated Carbon Observation System) present a significant advancement in the nearly continuous
⁴² observation of biogeochemical processes at the continental scale. Notably, at 47 terrestrial sites
⁴³ across the continental United States that span 20 ecoclimatic domains, NEON provides half-
⁴⁴ hourly measurements of soil CO₂ concentration, temperature, and moisture at different vertical
⁴⁵ depths. Each of these NEON sites also encompasses measurements of the cumulative sum of all
⁴⁶ ecosystem carbon fluxes in an airshed using the eddy covariance technique (Balocchi, 2014).

47 Soil observations provided by NEON are on the same timescale and standardized with eddy co-
48 variance measurements from FLUXNET. These types of nearly continuous observational data
49 (NEON and FLUXNET) can be used to reconcile differences between model-derived or data-
50 estimated components of ecosystem carbon flux (Jian et al., 2022; Luo et al., 2011; Phillips et
51 al., 2017; J. Shao et al., 2015; P. Shao et al., 2013; Sihl et al., 2016).

52 Estimated or observed soil carbon fluxes are a key metric for understanding change in soil
53 carbon pools over time (Bond-Lamberty et al., 2024). A soil carbon flux to the atmosphere
54 (F_S , units $\mu\text{mol m}^{-2} \text{ s}^{-1}$), represents the aggregate process of transfer of soil CO_2 to the
55 atmosphere from physical and biological processes (e.g. diffusion and respiration). Soil carbon
56 fluxes can be assumed to encompass soil carbon respiration from autotrophic or heterotrophic
57 sources (Davidson et al., 2006) and modeled with a exponential Q_{10} paradigm (Bond-Lamberty
58 et al., 2004; Chen & Tian, 2005; Hamdi et al., 2013).

59 One common method by which F_S is measured in the field is through the use of soil chambers
60 in a closed, well-mixed system (Norman et al., 1997) with headspace trace gas concentrations
61 measured with an infrared gas analyzer (IRGA). F_S can also be estimated from soil CO_2
62 measurements at different depths in the soil using the flux-gradient method (Maier & Schack-
63 Kirchner, 2014). Closed-chamber IRGA measurements, while being the most common method,
64 require either frequent in-person site visits or expensive and fragile automated systems. The
65 potential of the gradient method is that fluxes can be estimated from continuous data recorded
66 by robust solid-state sensors. The flux-gradient method is an approach that uses conservation
67 of mass to calculate flux at a vertical soil depth z at steady state by applying Fick's law of
68 diffusion. A simplifying assumption for the flux-gradient method is that there is no mass trans-
69 fer in the other spatial dimensions x and y (Maier & Schack-Kirchner, 2014). The diffusivity
70 profile, a key component of this calculation, varies across the soil depth as a function of soil
71 temperature, soil volumetric water content, atmospheric air pressure, and soil bulk density

72 (Millington & Shearer, 1971; Moldrup et al., 1999; Sallam et al., 1984).

73 Databases such as the Soil Respiration Database (SRDB) or the Continuous Soil Respiration
74 Database (COSORE) add to the growing network of resources for making collected observa-
75 tions of soil fluxes available to other researchers (Bond-Lamberty, 2018; Bond-Lamberty et
76 al., 2020; Bond-Lamberty & Thomson, 2010; Jian et al., 2021; Jiang et al., 2024). However,
77 these databases currently encompass primarily direct soil measurements of fluxes (i.e. those
78 using methods like the closed-chamber method described above). Currently, NEON provides
79 all measurements to calculate F_S from Fick's law, but soil flux as a derived data product was
80 descoped from the initial network launch due to budget constraints (Berenbaum et al., 2015).
81 Deriving estimates of F_S using continuous sensor data across NEON sites using NEON data
82 thus remains a high priority.

83 This study describes an R software package, `neonSoilFlux`, that computes a standardized
84 estimate of F_S at all terrestrial NEON sites using the flux-gradient method. Using direct
85 chamber-based field observations of soil carbon dioxide flux from a subset of terrestrial NEON
86 sites spanning six states, we provide a direct validation of F_S from `neonSoilFlux`. While
87 open source R software tools currently exist for processing chamber-based flux measurements
88 (Jurasinski et al., 2022; Pedersen, 2024; Rheault et al., 2024; Wilson et al., 2024; Zhao, 2019),
89 to our knowledge this is the first package that incorporates NEON data directly.

90 Key objectives of this study are to:

- 91 1. Apply the flux-gradient method to estimate soil CO₂ flux from continuous sensor mea-
92 surements across six NEON sites.
- 93 2. Benchmark estimated soil carbon fluxes against field measurements (e.g. direct chamber
94 measurements of soil flux).

95 3. Identify sources of error in the flux-gradient approach across diverse sites in order to
96 guide future work.

97 **3 Materials and Methods**

98 **3.1 Field methods**

99 **3.1.1 Focal NEON Sites**

100 In order to acquire field data to validate model predictions of flux, we selected six terrestrial
101 NEON sites for analysis. We conducted roughly week-long field measurement campaigns at
102 these sites, which span a range of environmental gradients and terrestrial domains (Table 1).
103 SJER, SRER, and WREF were visited during May and June of 2022, and WOOD, KONZ,
104 and UNDE during May and June of 2024. Permits or waivers were sought and approved prior
105 to field work at all six sites. In 2022, research activities were conducted whole or in part on
106 the Wind River Experimental Forest within the Gifford Pinchot National Forest. No permit
107 was required for this work. Approval for research at San Joaquin Experimental Range was
108 granted by Dr. Angela White in May 2022 and for research at Santa Rita Experimental Range
109 by Dr. Mitch McClaran in May 2022. In 2024, permits were received for work at WOOD
110 (Chase Lake WMD; permit number 62515-24-020), KONZ (Konza Prairie Biological Station;
111 permit number 766), and UNDE (University of Notre Dame Environmental Research Center;
112 permit number UNDERC-2024-5).

113 **3.1.2 Soil collar placement**

114 Either one (2022 sampling campaign) or two (2024 sampling campaign) PVC soil collars (20.1
115 cm inside diameter) were installed in close proximity to the permanent NEON soil sensors at
116 each site (Figure 1). As instruments in the NEON soil sensor arrays can occasionally break
117 down or stop working, the specific soil plot where we made measurements was chosen at each
118 site in consultation with NEON staff to maximize likelihood of quality soil sensor measurements
119 during the duration of the IRGA measurements. The plot selected at each site (out of the 5 in
120 each replicate array at each site) are presented in the last column of Table 1. After installation,
121 collar(s) were left to equilibrate for approximately 24 hours prior to any measurements being
122 taken.

123 **3.1.3 Infrared gas analyzer measurements of soil CO₂ flux**

124 In 2022, we then made measurements of flux on an hourly interval for 8 hours each day.
125 Measurements were taken from roughly 8 am to 4 pm, with the time interval selected to
126 capture the majority of the diurnal gradient of soil temperature each day. These measurements
127 were made using a LI-6800 infrared gas analyzer instrument (LI-COR Environmental, Lincoln,
128 NE) fitted with a soil chamber attachment (attachment 6800-09). In 2024, we again used the
129 same LI-6800 instrument, but made half-hourly measurements over an approximately 8 hour
130 period. In addition, in 2024 we also installed a second collar and used a second instrument, an
131 LI-870 CO₂ IRGA, connected to an automated robotic chamber (LI-COR chamber 8200-104)
132 controlled by an LI-8250 multiplexer to make automated measurements. The multiplexer was
133 configured to take half-hourly measurements 24 hours a day for the duration of our sampling
134 bout at each site. Each instrument was paired with a soil temperature and moisture probe
135 (Stevens HydraProbe, Stevens Water, Portland, OR) that was used to make soil temperature
136 and moisture measurements concurrent with the CO₂ flux measurements. Chamber volumes

were set by measuring collar offsets at each site. System checks were conducted daily for the LI-6800 and weekly for the LI-8250. Instruments were factory calibrated before each field season.



Figure 1: Spatial layout of field sampling using a closed-dynamic chamber setup at a representative NEON site (KONZ). Left image shows collars (white arrows) and permanent soil sensor installation (black arrow) and right image shows the LI-6800 (foreground) and LI-8200-104 (background) instruments placed on the collars.

Table 1: Listing of NEON sites studied for field work and analysis. Site refers to NEON site codes: Santa Rita Experimental Range (SRER), San Joaquin Experimental Range (SJER), Wind River Experimental Forest (WREF), Chase Lake National Wildlife Refuge (WOOD), Konza Prairie Biological Station (KONZ), and the University of Notre Dame Environmental Research Center (UNDE). Location is reported in decimal degrees of latitude and longitude. Other abbreviations include Mean Annual Temperature (MAT); \bar{T}_S : average soil temperature during field measurements; \overline{SWC} : average soil water content during field measurements. Dates refer to field measurement dates for each site. Plot refers to the particular location in the soil sensor array (denoted as HOR by NEON) where field measurements were made.

Site	Location	Ecosystem	MAT	\bar{T}_S	MAP	\overline{SWC}	Dates	Plot
SRER	31.91068, -110.83549	Shrubland	19.3 °C	47.6 °C	346 mm	4.0%	May 29– June 1 2022	004
SJER	37.10878, -119.73228	Oak woodland	16.4 °C	41.7 °C	540 mm	1.2%	June 1–4 2022	005
WREF	45.82049, -121.95191	Evergreen forest	9.2 °C	15.3 °C	2225 mm	27.2%	June 7–9 2022	001

Table 1: Listing of NEON sites studied for field work and analysis. Site refers to NEON site codes: Santa Rita Experimental Range (SRER), San Joaquin Experimental Range (SJER), Wind River Experimental Forest (WREF), Chase Lake National Wildlife Refuge (WOOD), Konza Prairie Biological Station (KONZ), and the University of Notre Dame Environmental Research Center (UNDE). Location is reported in decimal degrees of latitude and longitude. Other abbreviations include Mean Annual Temperature (MAT); \bar{T}_S : average soil temperature during field measurements; \bar{SWC} : average soil water content during field measurements. Dates refer to field measurement dates for each site. Plot refers to the particular location in the soil sensor array (denoted as HOR by NEON) where field measurements were made.

Site	Location	Ecosystem	MAT	\bar{T}_S	MAP	\bar{SWC}	Dates	Plot
WOOD	47.1282, -99.241334	Restored prairie	4.9 °C	14.9 °C	495 mm	14.9%	June 3–9 2024	001
KONZ	39.100774, -96.563075	Tallgrass prairie	12.4 °C	23.4 °C	870 mm	23.4%	May 29– June 1 2024	001
UNDE	46.23391, -89.537254	Deciduous forest	4.3 °C	13.0 °C	802 mm	13.0%	May 22–25 2024	004

3.1.4 Post-collection processing of field data

We used LI-COR SoilFluxPro software (v 5.3.1) to assess the data after collection and to inform sampling parameters. We checked appropriateness of dead band and measurement durations using built-in evaluation tools. Based on this, the deadband period was set for 30-40 seconds, depending on the site, and the measurement duration was 180 seconds with a 30 second pre-purge and a 30 second post-purge at most sites, and a 90 second pre- and post-purge at sites with higher humidity due to recent precipitation events. We also assessed the R^2 of linear and exponential model fits to measured CO₂ to verify measurement quality.

3.2 neonSoilFlux R package

We developed an R package called `neonSoilFlux` (Zobitz et al., 2024) to compute half-hourly soil carbon fluxes and uncertainties from NEON data. The objective of the `neonSoilFlux`

151 package is a unified workflow (Figure 2) for soil data acquisition and analysis that supplements
152 the existing `neonUtilities` data acquisition R package (Lunch et al., 2025).

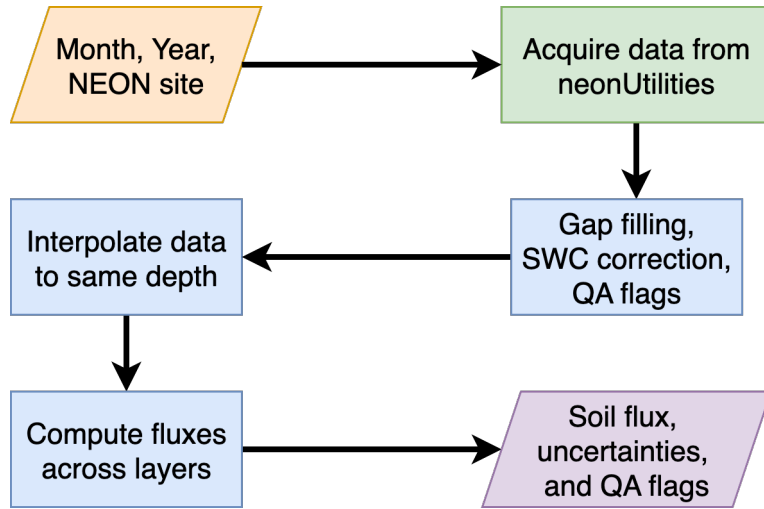


Figure 2: Diagram of `neonSoilFlux` R package. For a given month, year, and NEON site (orange parallelogram), the package acquires all relevant data to compute F_S using the `neonUtilities` R package (green rectangle). Data are gap-filled according to reported QA flags and adjusted for changes in soil water content (SWC) calibration coefficients, then interpolated to the same measurement depth before computing the soil flux, uncertainties, and final QA flags (blue rectangles). The package reports the associated soil flux, uncertainties, and quality assurance (QA) flags for the user (purple parallelogram).

153 At a given NEON site there are five replicate soil plots, each with measurements of soil
154 CO_2 concentration, soil temperature, and soil moisture at different depths (Figure 3). The
155 `neonSoilFlux` package acquires measured soil CO_2 concentration (NEON, 2024b), soil tem-
156 perature (NEON, 2024d), soil water content (NEON, 2024e), barometric pressure from the
157 nearby tower (NEON, 2024a), and soil properties (e.g. bulk density) (NEON, 2024c) from a
158 range of different NEON data products. The static soil properties were collected by NEON
159 staff from a nearby soil pit during initial site characterization and are assumed to be constant
160 at each site. A soil flux calculation is computed at each replicate soil plot.

161 The workflow to compute a value of F_S with `neonSoilFlux` consists of three primary steps,

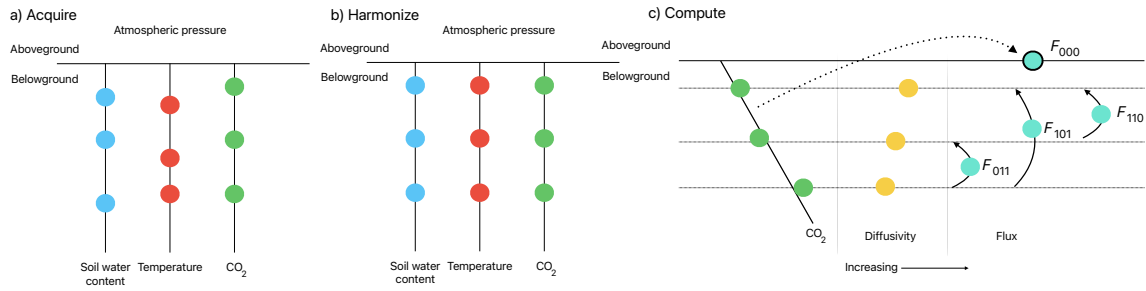


Figure 3: Model diagram of the data workflow for the `neonSoilFlux` R package. a) Acquire: Data are obtained for a given NEON location and horizontal sensor location, which includes soil water content, soil temperature, CO₂ concentration, and atmospheric pressure. All data are screened for quality assurance; if gap-filling of missing data occurs, it is flagged for the user. b) Harmonize: Any belowground data are then harmonized to the same depth as CO₂ concentrations using linear regression. c) Compute: The flux across a given depth is computed via Fick's law, denoted with F_{ijk} , where i , j , or k are either 0 or 1 denoting the layers the flux is computed across (i = closest to surface, k = deepest). F_{000} represents a flux estimate where the gradient dC/dz is the slope of a linear regression of CO₂ with depth.

illustrated in Figure 3. First, NEON data are acquired for a given site and month via the `neonUtilities` R package (yellow parallelogram and green rectangle in Figure 2 and Panel a in Figure 3). Acquired environmental data can be exported to a comma separated value file for additional analysis. Quality assurance (QA) flags are reported as an indicator variable. Since the calibration coefficients on the soil water content sensors have changed over time (NEON, 2024e), raw sensor measurements were back-calculated and soil-specific calibrations were applied following Ayres et al. (2024) to generate a consistent time series at each measurement location.

The second step is harmonizing the data to compute soil fluxes across soil layers. This step consists of three different actions (blue rectangles in Figure 2 and Panel b in Figure 3). If a given observation by NEON is reported as not passing a quality assurance check, we applied a gap filling method to replace that measurement with its monthly mean at that same depth (Section 3.2.1). Belowground measurements of soil water and soil temperature are then inter-

175 polated to the same depth as soil CO₂ measurements. The diffusivity (Section 3.2.2) and soil
176 flux across different soil layers (Section 3.2.3) are then computed.

177 The third and final step is computing a surface soil flux through extrapolation to the sur-
178 face (purple parallelogram in Figure 2 and Panel c in Figure 3). Uncertainty on a soil flux
179 measurement is computed through quadrature. An aggregate quality assurance (QA) flag
180 for each environmental measurement is also reported, representing if any gap-filled measure-
181 ments were used in the computation of a soil flux. Within the soil flux-gradient method,
182 several different approaches can be used to derive a surface flux (Maier & Schack-Kirchner,
183 2014); the `neonSoilFlux` package reports four different possible values for soil surface flux
184 (Section 3.2.3) for each of two different methods of diffusivity estimation, for a total of eight
185 estimates of flux.

186 **3.2.1 Gap-filling routine**

187 NEON reports QA flags as binary values for each measurement and half-hourly interval. For
188 a given half-hour, if any input variable (soil CO₂ concentration, soil temperature, or soil
189 moisture) at depth z is flagged, computation of F_S is not possible. To address this, flagged
190 measurements and their uncertainties were replaced with a bootstrapped monthly mean (\bar{m})
191 and monthly standard deviation (\bar{s}) (Efron & Tibshirani, 1994).

192 For each month, depth z , and variable, we computed bootstrapped estimates of \bar{m} and \bar{s}
193 from the vectors of unflagged measurements (**m**), reported standard errors (σ), and the 95%
194 confidence interval (ϵ , or expanded uncertainty; Farrance & Frenkel (2012)). We also defined
195 a bias vector $\mathbf{b} = \sqrt{\epsilon^2 - \sigma^2}$, which quantifies the spread of uncertainty in a given period and
196 is incorporated into \bar{m} .

197 From these, 5000 bootstrap samples were generated for \mathbf{m}, σ , and \mathbf{b} . For each sample
 198 (m_k, b_k, σ_k), we generated a vector \mathbf{n} (length $N = 5000$) by drawing from a normal dis-
 199 tribution with mean $m_k + b_k$ and standard deviation σ_k . The sample mean and standard
 200 deviation were then computed from \mathbf{n} . The resulting distributions of sample means and
 201 sample standard deviations provided the bootstrapped monthly mean (\bar{m}) and standard error
 202 (\bar{s}) respectively.

203 This gap-filling procedure provides a consistent treatment across all data streams. However,
 204 alternative approaches may be better suited for longer gaps (e.g., correlations with other
 205 NEON measurement levels or soil plots) or for variable-specific conditions. We discuss the
 206 effect of gap-filling on our results in Section 5.1.

207 **3.2.2 Soil diffusivity**

208 Soil diffusivity D_a at a given measurement depth is the product of the diffusivity in free air
 209 $D_{a,0}$ ($\text{m}^2 \text{ s}^{-1}$) and the tortuosity ξ (no units) (Millington & Shearer, 1971).

210 We compute $D_{a,0}$ with Equation 1:

$$D_{a,0} = 0.0000147 \cdot \left(\frac{T_i + 273.15}{293.15} \right)^{1.75} \cdot \left(\frac{P}{101.3} \right) \quad (1)$$

211 where T_i is soil temperature ($^\circ\text{C}$) at depth i (NEON, 2024d) and P surface barometric pressure
 212 (kPa) (NEON, 2024a).

213 Previous studies by Sallam et al. (1984) and Tang et al. (2003) demonstrated the sensitivity
 214 of modeled F_S depending on the tortuosity model (ξ) used to compute diffusivity. At low
 215 soil water content, the choice of tortuosity model can lead to order-of-magnitude differences

216 in D_a , which in turn affect modeled F_S . The `neonSoilFlux` package currently includes two
217 approaches to calculate ξ , representing the range of tortuosity behavior reported in Sallam et
218 al. (1984).

219 The first approach is the Millington-Quirk model (Millington & Shearer, 1971), in which
220 tortuosity depends on both porosity and soil water content:

$$\xi = \frac{(\phi - SWC_i)^{10/3}}{\phi^2} \quad (2)$$

221 In Equation 2, SWC is the soil water content at depth i (NEON, 2024e) and ϕ is the porosity,
222 which in turn is a function of soil physical properties (NEON, 2024c):

$$\phi = \left(1 - \frac{\rho_s}{\rho_m}\right) (1 - f_V) \quad (3)$$

223 In Equation 3, ρ_m is the particle density of mineral soil (2.65 g cm^{-3}), ρ_s the soil bulk density (g
224 cm^{-3}) excluding coarse fragments greater than 2 mm (NEON, 2024c), and f_V is a site-specific
225 value that accounts for the proportion of soil fragments between 2-20 mm. Soil fragments
226 greater than 20 mm were not estimated due to limitations in the amount of soil that can be
227 analyzed (NEON, 2024c). We assume that rock fragments contain no internal pores.

228 The Millington-Quirk model assumes ξ is modulated by the amount of fluid saturation in
229 soil pores (Millington & Shearer, 1971). In contrast, the Marshall model (Marshall, 1959)
230 expresses tortuosity as only a function of porosity ($\xi = \phi^{1.5}$), with ϕ defined from Equation
231 3. The Marshall model is independent of soil water content and assumes tortuosity is only
232 governed by soil structure. The `neonSoilFlux` package allows users to choose the tortuosity
233 model most appropriate for site-specific conditions and research goals.

234 **3.2.3 Soil flux computation**

235 We applied Fick's law (Equation 4) to compute the soil flux F_{ij} ($\mu\text{mol m}^{-2} \text{s}^{-1}$) across two
236 soil depths i and j :

$$F_{ij} = -D_a \frac{dC}{dz} \quad (4)$$

237 where D_a is the diffusivity ($\text{m}^2 \text{s}^{-1}$) and $\frac{dC}{dz}$ is the gradient of CO_2 molar concentration
238 ($\mu\text{mol m}^{-3}$, so the gradient has units of $\mu\text{mol m}^{-3} \text{m}^{-1}$). The soil surface flux is theoretically
239 defined by applying Equation 4 to measurements collected at the soil surface and directly
240 below the surface. Measurements of soil temperature, soil water content, and soil CO_2 molar
241 concentration across the soil profile allow for application of Equation 4 across different soil
242 depths. Each site had three measurement layers, so we denote the flux as a three-digit subscript
243 F_{ijk} with indicator variables i , j , and k indicate if a given layer was used (written in order of
244 increasing depth), according to the following:

- 245 • F_{000} is a surface flux estimate using the intercept of the linear regression of D_a with
246 depth and the slope from the linear regression of CO_2 with depth (which represents $\frac{dC}{dz}$
247 in Fick's Law). Tang et al. (2003) used this approach to compute fluxes in an oak-grass
248 savannah.
- 249 • F_{110} is a flux estimate across the two shallowest measurement layers.
- 250 • F_{011} is a flux estimate across the two deepest measurement layers.
- 251 • F_{101} is a flux estimate across the shallowest and deepest measurement layers.

252 For F_{110} , F_{011} , and F_{101} , the diffusivity used in Fick's Law is always at the deeper measurement
253 layer. When used as a surface flux estimate we assume CO_2 remains constant above this flux
254 depth. Uncertainty in all F_{ijk} values was quantified using quadrature (Taylor, 2022). These

255 computed fluxes could provide the basis for additional soil flux estimates. For example, Tang et
256 al. (2005) estimated surface flux by linearly extrapolating F_{110} and F_{011} to the soil surface.

257 **3.3 Post processing evaluation**

258 Following collection of field measurements and calculation of the soil fluxes from `neonSoilFlux`
259 package, we compared measured F_S based on closed-dynamic chamber measurements with the
260 LI-COR instruments to a given soil flux calculation from `neonSoilFlux` for each site and flux
261 computation method and quantified the relationship statistically (R^2). Finally, for a half-
262 hourly interval we also computed a *post hoc* diffusivity (D_a) using the LI-COR flux along
263 with the CO_2 surface gradient reported by NEON using the measurement levels closest to the
264 surface.

265 **4 Results**

266 **4.1 Concordance between modelled and measured soil CO_2 flux**

267 The sites we visited ranged substantially in both their annual average temperature and precip-
268 itation as well as their biome type (Table 2). These differences also influenced the wide range
269 of observed flux rates across sites.

270 The timeseries of the measured fluxes from the LI-COR 6800 and 870/8250 were compared
271 to modeled soil fluxes from the `neonSoilFlux` R package (Figure 4). We also assessed year-
272 long estimated flux time series and compared those to field measurements made at each site
273 (Figure 5). Results are reported in local time. Where applicable, sites are displayed from left
274 to right by increasing soil temperature (Table 1). Positive values of the flux indicate that there
275 is a flux moving towards the surface. Overall, with the exception of SRER (discussed later) the

Table 2: Summary of measured soil characteristics and flux results from field measurements across six NEON sites using a LI-COR 6800 (LI-870/8250 measurements omitted to enable direct comparability) via the closed-dynamic chamber method. Numeric values for soil CO₂ flux, soil temperature, and volumetric soil water content (VSWC) are the mean and standard deviation of field measurements at each site.

Site	Flux μmol m ⁻² s ⁻¹	Soil temp °C	VSWC cm ³ cm ⁻³	n
UNDE	2.55 ± 0.26	14.33 ± 0.77	0.33 ± 0.02	61
WOOD	3.02 ± 0.4	16.01 ± 1.54	0.28 ± 0.01	53
WREF	3.62 ± 0.3	15.34 ± 1.76	0.27 ± 0.06	21
KONZ	6.35 ± 0.97	27.28 ± 4.14	0.37 ± 0.01	44
SJER	0.94 ± 0.02	41.68 ± 11.22	0.01 ± 0.01	32
SRER	0.72 ± 0.09	47.64 ± 7.46	0.04 ± 0.01	32

276 computed fluxes determined using a variety of plausible methods spanned the field-measured
 277 fluxes, but the specific flux-gradient method that best approximated field measurements varied
 278 by site.

279 We calculated a statistical relationship between the various estimates of soil flux computed by
 280 `neonSoilFlux` and the field-measured fluxes within daily interval periods. Statistics for these
 281 comparisons are reported in Figure 6, which also shows how these fall relative to a 1:1 line.

282 4.2 Effects of method choice on diffusivity estimates

283 In one of the six field sites, the *post hoc* D_a estimate fell roughly between the two diffusion
 284 estimation methods. At UNDE, WOOD, WREF, and SJER, the median field estimate of
 285 diffusivity was lower than both of the other methods. At the driest site, SRER (Table 1),
 286 the median field estimate of diffusivity was higher than both of the other methods and values
 287 showed a large amount of variation (Figure 7).

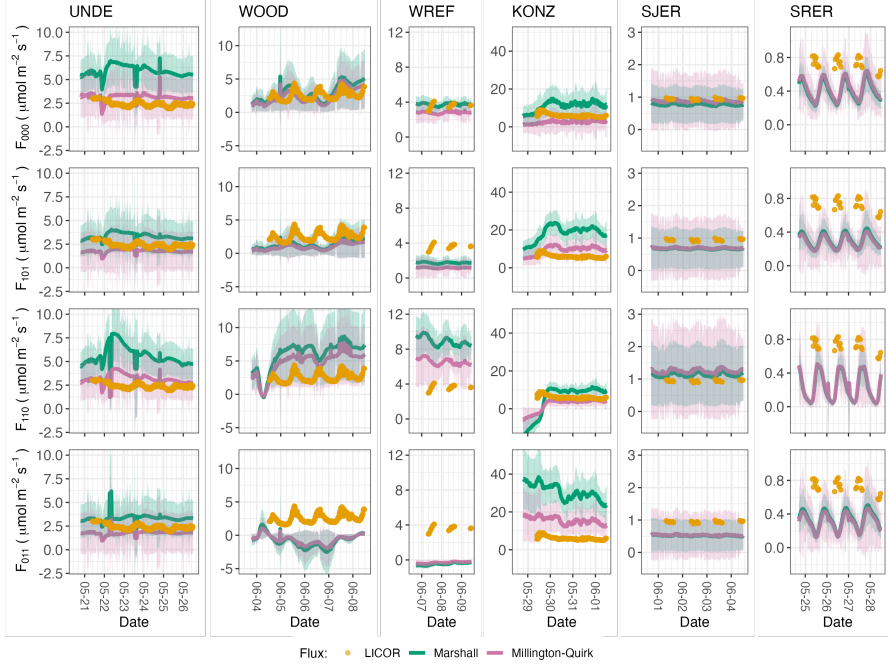


Figure 4: Timeseries of soil surface flux (F_S) from field-measured (yellow lines) and modeled soil fluxes (green or purple lines) by the `neonSoilFlux` R package. Fluxes from the `neonSoilFlux` R package are separated by the diffusivity model used (Millington-Quirk or Marshall, Section 3.2.2). Individual vertical axis labels in the first column represent the measurement levels where the flux-gradient approach is applied (Section 3.2.3). Ribbons for modeled soil fluxes represent approximately ± 1 standard deviation. Results are reported in local time. WREF, SJER, and SRER were sampled in 2022, and UNDE, WOOD, and KONZ were sampled in 2024. Sites (columns) are arranged from left to right in terms of increasing mean annual temperature.

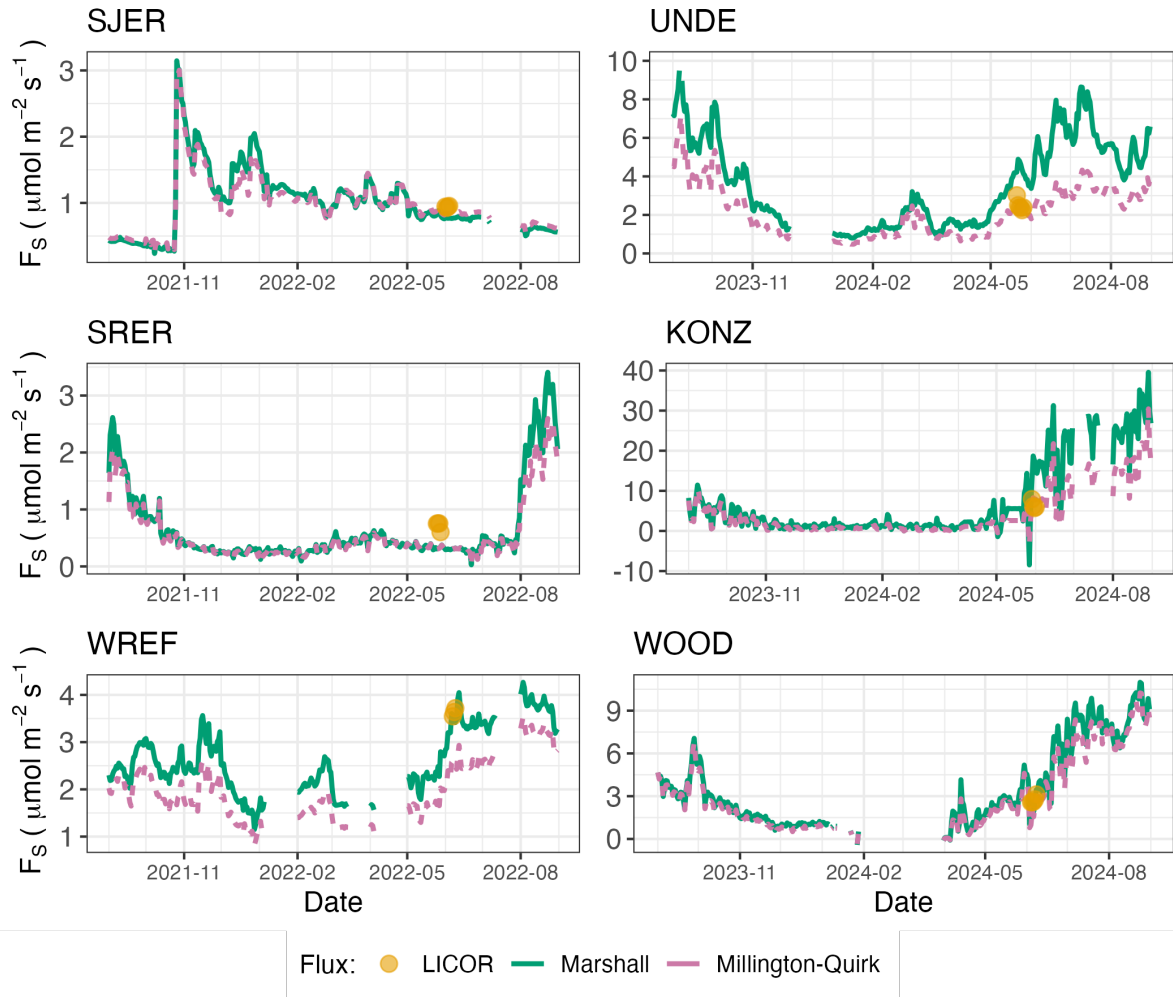


Figure 5: Timeseries of both daily-averaged field F_S (yellow circles) and daily ensemble averaged soil fluxes (average of F_{000} , F_{101} , F_{011} , F_{110} , Section 3.2.3) by the `neonSoilFlux` R package, separated by the diffusivity model used (green or purple lines, Millington-Quirk or Marshall, Section 3.2.2).

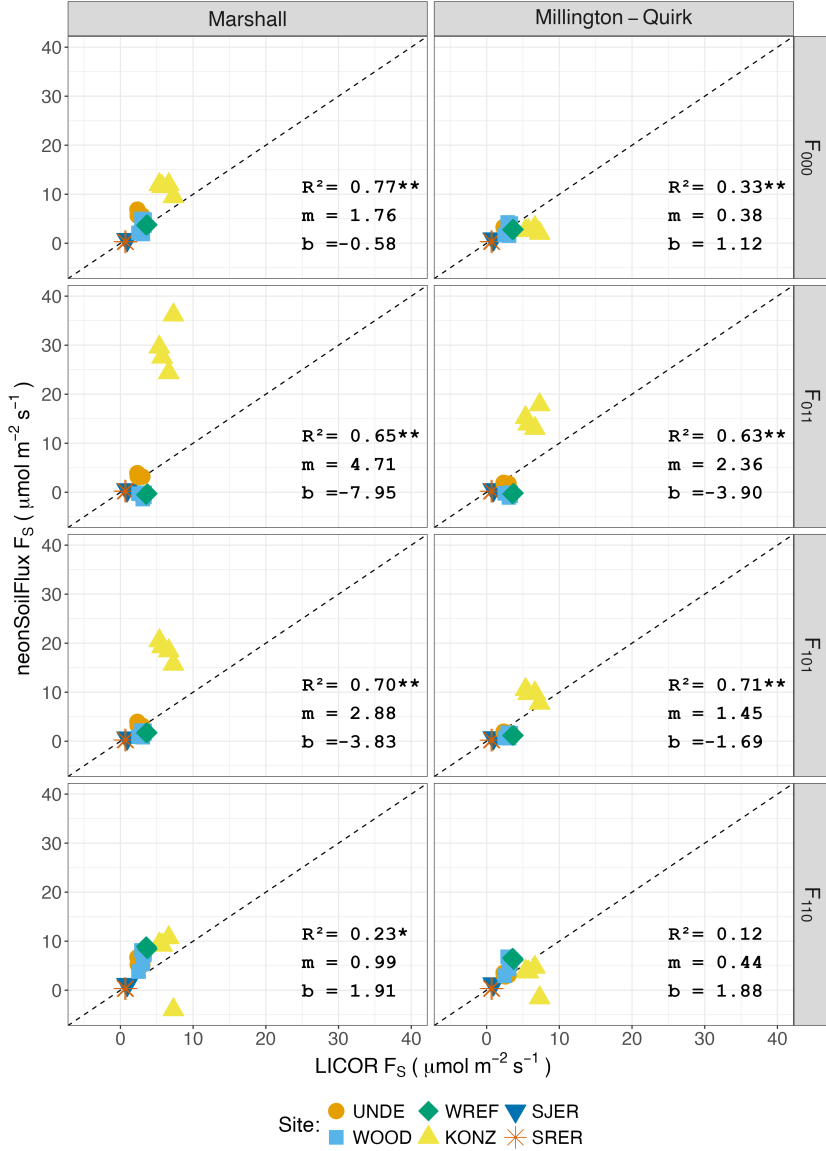


Figure 6: Statistical comparison between measured fluxes at each NEON site with fluxes reported by `neonSoilFlux` with the different flux calculation approaches and diffusivity calculations applied. Points are daily averages and LICOR F_S values are from the 6800 instrument only, for consistency. The dotted line represents a 1:1 relationship, and the reported R^2 quantifies the relationship between field-measured and `neonSoilFlux` estimated fluxes. * = significance at the 5% level, ** = significance at the 1% level. The slope (m) and intercept (b) of the linear regression between measured and modeled fluxes are also reported. The low-value outlier from KONZ in the F_{110} Marshall plot is an example of the effect of inverted CO₂ gradients causing an estimated flux to be negative, bringing down the daily mean, which later resolved as the soils dried back out.

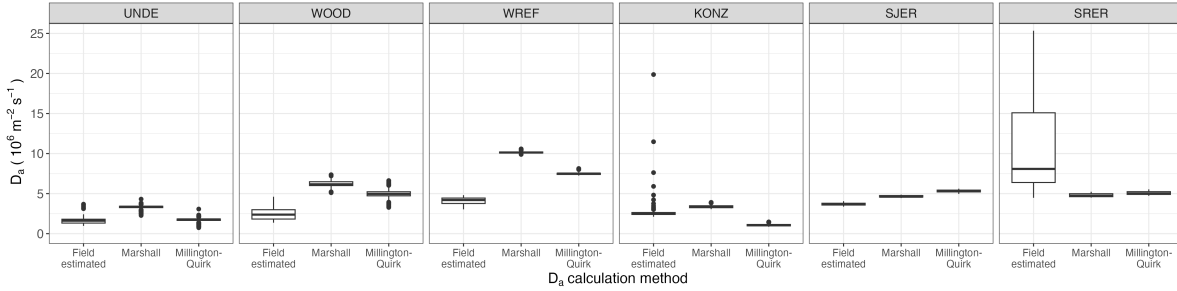


Figure 7: Distribution of diffusivity (D_a) at each study site. Values of D_a were provided by the `neonSoilFlux` package, computed from the Millington-Quirk or Marshall models (Section 3.2.2). A post-hoc estimate of diffusivity (labeled as “Field estimated”) was computed through the field measured flux (Figure 4), divided by the CO₂ gradient from the measurement levels closest to the soil surface, as reported by NEON. We only used F_S measured by the LICOR 6800 at all sites to standardize comparisons. Some outliers (n = 1 from the field estimated values at KONZ and n = 6 from field estimated values at SRER) are excluded from the plot to allow better comparative visualization across sites.

288 5 Discussion

289 This study presents a unified data science workflow to efficiently process automated measurements of belowground soil CO₂ concentrations, soil water content, and soil temperature to
 290 infer estimates of soil surface CO₂ effluxes through application of Fick’s Law (Equation 4).
 291 Our core goals in this study were: (1) to generate estimates of soil flux from continuous soil
 292 sensor data at terrestrial NEON sites using the flux-gradient method and then (2) to compare
 293 those estimates to field-measured fluxes based on the closed chamber approach at six NEON
 294 focal sites. We discuss our progress toward these core goals through (1) an overall evaluation
 295 of the flux-gradient approach (and uncertainty calculation) and (2) site-specific evaluation of
 296 differences in estimated vs measured fluxes.
 297

298 **5.1 General evaluation of flux-gradient approach**

299 Key assumptions of the flux-gradient approach are that CO₂ concentrations increase through-
300 out the soil profile such that the highest concentrations are observed in the deepest layers. Ad-
301 ditionally, field flux measurements should correlate with F_{000} because they represent surface
302 fluxes. Periods where this gradient condition are not met generally are connected to processes
303 that occur during soil wetting events, where more shallow soil layers produce higher concentra-
304 tions of CO₂ due to microbial respiration pulses following rewetting. This effect is likely to be
305 largest at sites with rich organic soils (e.g. KONZ). Based on this reasoning, in these types of
306 situations we would *a priori* expect F_{011} (deepest layers) $\leq F_{101} \leq F_{110}$ (shallow layers) \leq
307 F_{000} (all layers) because the previous flux estimates rely primarily on CO₂ concentrations at
308 deeper depths, and could miss high concentrations of CO₂ produced in shallower layers.

309 When modeling soil respiration, typically a non-linear response function that also considers soil
310 type is used (Bouma & Bryla, 2000; Yan et al., 2016, 2018). For the `neonSoilFlux` package,
311 soil type is connected to the measurement of bulk density, which was characterized at each
312 NEON site. This bulk density estimate is based on replicate samples collected from the site
313 megapit at a subset of soil horizons, with an estimated uncertainty of $\pm 5\%$ (NEON, 2024c).
314 Coarse fragment estimates also have very large uncertainties, but because the volume fraction
315 tends to be low in surface soils it is unlikely to contribute much additional flux uncertainty.

316 Our results suggest that the most important way to improve reliability of the flux estimate is
317 to reduce the usage of gap-filled data. The current approach to gap filling in `neonSoilFlux`
318 uses monthly mean data to gap fill—this approach decreases the ability of the estimate to
319 be responsive to short-term pulses that occur with rapid weather shifts. All sites had more
320 than 75% of half-hourly periods with no-gap filled measurements (Figure S1, Supplementary
321 Information). At five out of six sites (all except SRER), we used at least some gap-filled
322 measurements of Soil Water Content (SWC). At WREF, field data collection occurred following

323 a severe rainstorm, with soils at the beginning of the sampling week near their water holding
324 capacity, which can influence the soil moisture sensor accuracy. In general, we recommend
325 that whenever possible, knowledge of local field conditions should influence analysis decisions
326 in addition to any QA filtering protocols in the `neonSoilFlux` package.

327 We recognize that this gap-filling approach may lead to gap-filled values that are quite different
328 from the actual values, such as an underestimate of soil moisture following rain events. Further
329 extensions of the gap filling method could use more sophisticated gap-filling routines, similar to
330 what is used for net ecosystem carbon exchange (Falge et al., 2001; Liu et al., 2023; Mariethoz et
331 al., 2015; Moffat et al., 2007; Zhang et al., 2023). Additionally, since the deepest temperature
332 and soil moisture sensors are located below the deepest CO₂ sensors at NEON sites, it is
333 possible that excluding these deeper layers from consideration prior to analysis would lead to
334 a reduced need for gap filling. Future iterations of the `neonSoilFlux` package may incorporate
335 this as an option. The current gap-filling routine provides a consistent approach that can be
336 applied to each data stream, but further work may explore alternative gap-filling approaches.

337 **5.2 Evaluation of flux-gradient approach at each site**

338 Derived results from the `neonSoilFlux` package have patterns that are broadly consistent with
339 those directly measured in the field (Figure 4 and Figure 5), even though statistical comparisons
340 between the field-measured and `neonSoilFlux` values were quite variable (e.g. R^2 ranging
341 from 0.12 to 0.77; Figure 6). One advantage of the `neonSoilFlux` package is its ability to
342 calculate fluxes across different soil depths (Figure 3), which allows for additional site-specific
343 customization. We believe the package can provide a useful baseline estimate of soil fluxes
344 that can always be complemented through additional field measurements.

345 The six locations studied provide a range of case studies that suggest different considerations

may apply to different sites when applying the flux-gradient method. For example, the Santa Rita Experimental Range (SRER) is a desert site characterized by sandy soil, which also was the location of the highest field soil temperatures that we observed (Table 2). At SRER the flux across the top two layers (F_{110}) produced a pattern of soil flux most consistent with the observed field data. The remaining methods F_{101} , F_{011} , or F_{000} are derived from information taken from the deepest layer, which seems to have been decoupled from the surface layers both in terms of temperature and CO₂ concentration. This may be a general circumstance where there are large diurnal temperature extremes that rapidly change during the course of a day and overnight, leading to lags in the timing of when temperature increases propagate down to deeper soil layers.

Immediately prior to our visit to Konza Prairie (KONZ), that site that experienced a significant rain event that led to wet soils that gradually dried out over the course of our time there. This pulse of precipitation increased the soil CO₂ concentration at the top layer above the concentrations in lower layers, leading to negative estimated flux values at the start of the field sampling period. In this case it was only when the soil began to return to a baseline level that the assumptions of the flux-gradient method were again met.

Both of the previous cases also provide context for the variable statistical comparisons between field-measured soil fluxes and `neonSoilFlux` outputs (Figure 6). When considering systematic deployment of this method across a measurement network, there are a number of independent challenges that require careful consideration. There are clear tradeoffs between (1) accuracy of modeled fluxes (defined here as closeness to field-measured F_S and the uncertainty reduction factor ϵ), (2) precision (which could be defined by the signal to noise ratio), and (3) the choice of the diffusivity model (Section 3.2.2) or flux computation method (Section 3.2.3). We performed a sensitivity analysis to compare the impact of these factors (Figure S2, Supplemental Information).

Finally, comparing the effects of different diffusivity estimation methods on the match between modeled and measured fluxes (Figure 5) highlights the sensitivity of F_{ijk} to diffusivity. The comparison between diffusivity estimates compared to field estimated diffusivity (Figure 7) demonstrates that site parameters can dictate which measure of diffusivity is most likely to be accurate in a given environmental context. Site-specific differences are largely a reflection of differences in soil moisture across the sites (Table 1), as not all diffusivity estimation methods incorporate soil moisture equivalently. While we here have compares two approaches to calculate diffusivity (the Millington-Quirk and Marshall models), it may be valuable to evaluate other diffusivity models (e.g. the Moldrup model; Moldrup et al. (1999)) as well. Ultimately the choice of a particular diffusivity model could be determined based on knowledge of site-specific evaluations or a set of these models could be used to generate a model ensemble average as a means to trade precision for a more general approach.

5.3 Recommendations for future method development

The `neonSoilFlux` package provides several approaches to estimate soil flux using the gradient method. We believe these approaches enable the software to be used across a range of site-specific assumptions (Maier & Schack-Kirchner, 2014). We note, however, that this choice can have a determinative approach on the calculated values. Ensemble averaging approaches (Elshall et al., 2018; Raftery et al., 2005) may be one way to address this problem if the goal is to calculate fluxes using the same method at a diverse range of different sites. Two other ideas would be to apply machine learning algorithms (e.g. random forest) to generate a single flux estimate across diverse sites, or using co-located estimates of net ecosystem carbon exchange from eddy-flux towers to further constrain results or to assess soil flux results for plausibility (Phillips et al., 2017).

These challenges notwithstanding, the method used here and made available in the

395 `neonSoilFlux` R package has the potential to produce nearly continuous estimates of flux
396 across all terrestrial NEON sites. These estimates are a significant improvement on available
397 approaches to constrain the portion of ecosystem respiration attributable to the soil. This,
398 in turn, also aids in our ability to understand the soil contribution to the net ecosystem flux
399 measured at these sites using the co-located eddy flux towers.

400 **6 Conclusions**

401 We used the R package `neonSoilFlux` to estimate soil CO₂ fluxes with the flux-gradient
402 method using data from buried soil sensors at NEON terrestrial sites. We compared the
403 predicted fluxes to those measured directly using a field-based closed chamber approach. Soil
404 fluxes from `neonSoilFlux` were broadly effective at producing estimates of flux comparable
405 to those measured in the field using a chamber-based technique. However `neonSoilFlux`
406 outputs are quite sensitive to a number of issues, including: missing data (and thus gap-
407 filling of input measurement datasets), the selection of soil depths used to best calculate the
408 gradient (which may vary between sites), and finally the choice of method used for estimating
409 soil diffusivity. The flexibility of the `neonSoilFlux` package allows the user to evaluate each
410 of these issues with site-specific knowledge and contexts. Future refinements and subsequent
411 validation of `neonSoilFlux` outputs will feed forward into evaluating soil carbon fluxes broader
412 spatial scales to enhance understanding of the ways in which soils across diverse ecosystems
413 are responding to a changing climate.

⁴¹⁴ **Sources Cited**

- ⁴¹⁵ Ayres, E., Reichle, R. H., Colliander, A., Cosh, M. H., & Smith, L. (2024). Validation of
⁴¹⁶ Remotely Sensed and Modeled Soil Moisture at Forested and Unforested NEON Sites.
⁴¹⁷ *IEEE Journal of Selected Topics in Applied Earth Observations and Remote Sensing*, 17,
⁴¹⁸ 14248–14264. <https://doi.org/10.1109/JSTARS.2024.3430928>
- ⁴¹⁹ Baldocchi, D. (2014). Measuring fluxes of trace gases and energy between ecosystems and the
⁴²⁰ atmosphere - the state and future of the eddy covariance method. *Global Change Biology*,
⁴²¹ 20(12), 3600–3609. <https://doi.org/10.1111/gcb.12649>
- ⁴²² Berenbaum, M. R., Carpenter, S. R., Hampton, S. E., Running, S. W., & Stanzione, D. C.
⁴²³ (2015). *Report from the NSF BIO Advisory Committee Subcommittee on NEON Scope
424 Impacts*.
- ⁴²⁵ Bond-Lamberty, B. (2018). New Techniques and Data for Understanding the Global Soil Res-
⁴²⁶piration Flux. *Earth's Future*, 6(9), 1176–1180. <https://doi.org/10.1029/2018EF000866>
- ⁴²⁷ Bond-Lamberty, B., Ballantyne, A., Berryman, E., Fluet-Chouinard, E., Jian, J., Morris, K.
⁴²⁸ A., Rey, A., & Vargas, R. (2024). Twenty Years of Progress, Challenges, and Opportuni-
⁴²⁹ties in Measuring and Understanding Soil Respiration. *Journal of Geophysical Research:
430 Biogeosciences*, 129(2), e2023JG007637. <https://doi.org/10.1029/2023JG007637>
- ⁴³¹ Bond-Lamberty, B., Christianson, D. S., Malhotra, A., Pennington, S. C., Sihi, D., AghaK-
⁴³²ouchak, A., Anjileli, H., Altaf Arain, M., Armesto, J. J., Ashraf, S., Ataka, M., Baldocchi,
⁴³³ D., Andrew Black, T., Buchmann, N., Carbone, M. S., Chang, S.-C., Crill, P., Curtis, P.
⁴³⁴ S., Davidson, E. A., ... Zou, J. (2020). COSORE: A community database for continuous
⁴³⁵ soil respiration and other soil-atmosphere greenhouse gas flux data. *Global Change Biology*,
⁴³⁶ 26(12), 7268–7283. <https://doi.org/10.1111/gcb.15353>
- ⁴³⁷ Bond-Lamberty, B., & Thomson, A. (2010). A global database of soil respiration data. *Bio-
438 geosciences*, 7(6), 1915–1926. <https://doi.org/10.5194/bg-7-1915-2010>

- 439 Bond-Lamberty, B., Wang, C., & Gower, S. T. (2004). A global relationship between the
440 heterotrophic and autotrophic components of soil respiration? *Global Change Biology*,
441 10(10), 1756–1766. <https://doi.org/10.1111/j.1365-2486.2004.00816.x>
- 442 Bouma, T. J., & Bryla, D. R. (2000). On the assessment of root and soil respiration for soils
443 of different textures: Interactions with soil moisture contents and soil CO₂ concentrations.
444 *Plant and Soil*, 227(1), 215–221. <https://doi.org/10.1023/A:1026502414977>
- 445 Chen, H., & Tian, H.-Q. (2005). Does a General Temperature-Dependent Q10 Model of Soil
446 Respiration Exist at Biome and Global Scale? *Journal of Integrative Plant Biology*, 47(11),
447 1288–1302. <https://doi.org/10.1111/j.1744-7909.2005.00211.x>
- 448 Davidson, E. A., Janssens, I. A., & Luo, Y. (2006). On the variability of respiration in
449 terrestrial ecosystems: Moving beyond Q10. *Global Change Biology*, 12, 154–164. <https://doi.org/10.1111/j.1365-2486.2005.01065.x>
- 450 Desai, A. R., Murphy, B. A., Wiesner, S., Thom, J., Butterworth, B. J., Koupaei-Abyazani, N.,
451 Muttaqin, A., Paleri, S., Talib, A., Turner, J., Mineau, J., Merrelli, A., Stoy, P., & Davis,
452 K. (2022). Drivers of Decadal Carbon Fluxes Across Temperate Ecosystems. *Journal of
453 Geophysical Research: Biogeosciences*, 127(12), e2022JG007014. <https://doi.org/10.1029/2022JG007014>
- 454 455 Efron, B., & Tibshirani, R. J. (1994). *An Introduction to the Bootstrap*. Chapman and
456 Hall/CRC. <https://doi.org/10.1201/9780429246593>
- 457 Elshall, A. S., Ye, M., Pei, Y., Zhang, F., Niu, G.-Y., & Barron-Gafford, G. A. (2018). Relative
458 model score: A scoring rule for evaluating ensemble simulations with application to micro-
459 bial soil respiration modeling. *Stochastic Environmental Research and Risk Assessment*,
460 32(10), 2809–2819. <https://doi.org/10.1007/s00477-018-1592-3>
- 461 Falge, E., Baldocchi, D., Olson, R., Anthoni, P., Aubinet, M., Bernhofer, C., Burba, G.,
462 Ceulemans, R., Clement, R., Dolman, H., Granier, A., Gross, P., Grünwald, T., Hollinger,
463 D., Jensen, N.-O., Katul, G., Keronen, P., Kowalski, A., Lai, C. T., ... Wofsy, S. (2001).
- 464

- 465 Gap filling strategies for defensible annual sums of net ecosystem exchange. *Agricultural*
466 and *Forest Meteorology*, 107(1), 43–69. [https://doi.org/10.1016/S0168-1923\(00\)00225-2](https://doi.org/10.1016/S0168-1923(00)00225-2)
- 467 Farrance, I., & Frenkel, R. (2012). *Uncertainty of Measurement: A Review of the Rules*
468 for Calculating Uncertainty Components through Functional Relationships. *The Clinical*
469 *Biochemist Reviews*, 33(2), 49–75.
- 470 Friedlingstein, P., O’Sullivan, M., Jones, M. W., Andrew, R. M., Hauck, J., Landschützer,
471 P., Le Quéré, C., Li, H., Luijkx, I. T., Olsen, A., Peters, G. P., Peters, W., Pongratz,
472 J., Schwingshackl, C., Sitch, S., Canadell, J. G., Ciais, P., Jackson, R. B., Alin, S. R., ...
473 Zeng, J. (2025). Global Carbon Budget 2024. *Earth System Science Data*, 17(3), 965–1039.
474 <https://doi.org/10.5194/essd-17-965-2025>
- 475 Hamdi, S., Moyano, F., Sall, S., Bernoux, M., & Chevallier, T. (2013). Synthesis analysis
476 of the temperature sensitivity of soil respiration from laboratory studies in relation to
477 incubation methods and soil conditions. *Soil Biology and Biochemistry*, 58, 115–126. <https://doi.org/10.1016/j.soilbio.2012.11.012>
- 479 Jackson, R. B., Lajtha, K., Crow, S. E., Hugelius, G., Kramer, M. G., & Piñeiro, G. (2017).
480 The Ecology of Soil Carbon: Pools, Vulnerabilities, and Biotic and Abiotic Controls.
481 *Annual Review of Ecology, Evolution and Systematics*, 48(Volume 48, 2017), 419–445.
482 <https://doi.org/10.1146/annurev-ecolsys-112414-054234>
- 483 Jian, J., Bailey, V., Dorheim, K., Konings, A. G., Hao, D., Shiklomanov, A. N., Snyder, A.,
484 Steele, M., Teramoto, M., Vargas, R., & Bond-Lamberty, B. (2022). Historically inconsis-
485 tent productivity and respiration fluxes in the global terrestrial carbon cycle. *Nature*
486 *Communications*, 13(1), 1733. <https://doi.org/10.1038/s41467-022-29391-5>
- 487 Jian, J., Vargas, R., Anderson-Teixeira, K., Stell, E., Herrmann, V., Horn, M., Kholod, N.,
488 Manzon, J., Marchesi, R., Paredes, D., & Bond-Lamberty, B. (2021). A restructured and
489 updated global soil respiration database (SRDB-V5). *Earth System Science Data*, 13(2),
490 255–267. <https://doi.org/10.5194/essd-13-255-2021>

- 491 Jiang, J., Feng, L., Hu, J., Liu, H., Zhu, C., Chen, B., & Chen, T. (2024). Global soil
492 respiration predictions with associated uncertainties from different spatio-temporal data
493 subsets. *Ecological Informatics*, 82, 102777. <https://doi.org/10.1016/j.ecoinf.2024.102777>
- 494 Jobbágy, E. G., & Jackson, R. B. (2000). The Vertical Distribution of Soil Organic Carbon
495 and its Relation to Climate and Vegetation. *Ecological Applications*, 10(2), 423–436. [https://doi.org/10.1890/1051-0761\(2000\)010%5B0423:TVDOSO%5D2.0.CO;2](https://doi.org/10.1890/1051-0761(2000)010%5B0423:TVDOSO%5D2.0.CO;2)
- 496 Jurasinski, G., Koebisch, F., Guenther, A., & Beetz, S. (2022). *Flux: Flux Rate Calculation
497 from Dynamic Closed Chamber Measurements*. <https://doi.org/10.32614/CRAN.package.flux>
- 498
- 500 Liu, K., Li, X., Wang, S., & Zhang, H. (2023). A robust gap-filling approach for European
501 Space Agency Climate Change Initiative (ESA CCI) soil moisture integrating satellite
502 observations, model-driven knowledge, and spatiotemporal machine learning. *Hydrology
503 and Earth System Sciences*, 27(2), 577–598. <https://doi.org/10.5194/hess-27-577-2023>
- 504 Lunch, C., Laney, C., Mietkiewicz, N., Sokol, E., Cawley, K., & Network), N. (National. E. O.
505 (2025). *neonUtilities: Utilities for Working with NEON Data*. <https://doi.org/10.32614/CRAN.package.neonUtilities>
- 506
- 507 Luo, Y., Ogle, K., Tucker, C., Fei, S., Gao, C., LaDeau, S., Clark, J. S., & Schimel, D. S. (2011).
508 Ecological forecasting and data assimilation in a data-rich era. *Ecological Applications*,
509 21(5), 1429–1442. <https://doi.org/10.1890/09-1275.1>
- 510 Maier, M., & Schack-Kirchner, H. (2014). Using the gradient method to determine soil gas
511 flux: A review. *Agricultural and Forest Meteorology*, 192–193, 78–95. <https://doi.org/10.1016/j.agrformet.2014.03.006>
- 512
- 513 Mariethoz, G., Linde, N., Jougnot, D., & Rezaee, H. (2015). Feature-preserving interpolation
514 and filtering of environmental time series. *Environmental Modelling & Software*, 72, 71–76.
515 <https://doi.org/10.1016/j.envsoft.2015.07.001>
- 516 Marshall, T. J. (1959). The Diffusion of Gases Through Porous Media. *Journal of Soil Science*,

- 517 10(1), 79–82. <https://doi.org/10.1111/j.1365-2389.1959.tb00667.x>
- 518 Millington, R. J., & Shearer, R. C. (1971). Diffusion in aggregated porous media. *Soil Science*,
519 111(6), 372–378.
- 520 Moffat, A. M., Papale, D., Reichstein, M., Hollinger, D. Y., Richardson, A. D., Barr, A. G.,
521 Beckstein, C., Braswell, B. H., Churkina, G., Desai, A. R., Falge, E., Gove, J. H., Heimann,
522 M., Hui, D., Jarvis, A. J., Kattge, J., Noormets, A., & Stauch, V. J. (2007). Comprehensive
523 comparison of gap-filling techniques for eddy covariance net carbon fluxes. *Agricultural and
524 Forest Meteorology*, 147(3), 209–232. <https://doi.org/10.1016/j.agrformet.2007.08.011>
- 525 Moldrup, P., Olesen, T., Yamaguchi, T., Schjønning, P., & Rolston, D. E. (1999). Modeling
526 diffusion and reaction in soils: 9. The Buckingham-Burdine-Campbell equation for gas
527 diffusivity in undisturbed soil. *Soil Science*, 164(2), 75.
- 528 NEON. (2024a). *Barometric pressure (DP1.00004.001)*. National Ecological Observatory
529 Network (NEON). <https://doi.org/10.48443/RT4V-KZ04>
- 530 NEON. (2024b). *Soil CO₂ concentration (DP1.00095.001)*. National Ecological Observatory
531 Network (NEON). <https://doi.org/10.48443/E7GR-6G94>
- 532 NEON. (2024c). *Soil physical and chemical properties, Megapit (DP1.00096.001)*. National
533 Ecological Observatory Network (NEON). <https://doi.org/10.48443/S6ND-Q840>
- 534 NEON. (2024d). *Soil temperature (DP1.00041.001)*. National Ecological Observatory Network
535 (NEON). <https://doi.org/10.48443/Q24X-PW21>
- 536 NEON. (2024e). *Soil water content and water salinity (DP1.00094.001)*. National Ecological
537 Observatory Network (NEON). <https://doi.org/10.48443/A8VY-Y813>
- 538 Norman, J. M., Kucharik, C. J., Gower, S. T., Baldocchi, D. D., Crill, P. M., Rayment, M.,
539 Savage, K., & Striegl, R. G. (1997). A comparison of six methods for measuring soil-
540 surface carbon dioxide fluxes. *Journal of Geophysical Research: Atmospheres*, 102(D24),
541 28771–28777. <https://doi.org/10.1029/97JD01440>
- 542 Pedersen, A. R. (2024). *HMR: Flux Estimation with Static Chamber Data*. <https://doi.org/>

- 543 [10.32614/CRAN.package.HMR](https://doi.org/10.32614/CRAN.package.HMR)
- 544 Phillips, C. L., Bond-Lamberty, B., Desai, A. R., Lavoie, M., Risk, D., Tang, J., Todd-Brown,
545 K., & Vargas, R. (2017). The value of soil respiration measurements for interpreting and
546 modeling terrestrial carbon cycling. *Plant and Soil*, 413(1), 1–25. <https://doi.org/10.1007/s11104-016-3084-x>
- 547
- 548 Raftery, A. E., Gneiting, T., Balabdaoui, F., & Polakowski, M. (2005). *Using Bayesian Model
549 Averaging to Calibrate Forecast Ensembles*. <https://doi.org/10.1175/MWR2906.1>
- 550 Rheault, K., Christiansen, J. R., & Larsen, K. S. (2024). goFlux: A user-friendly way to
551 calculate GHG fluxes yourself, regardless of user experience. *Journal of Open Source
552 Software*, 9(96), 6393. <https://doi.org/10.21105/joss.06393>
- 553 Sallam, A., Jury, W. A., & Letey, J. (1984). Measurement of Gas Diffusion Coefficient under
554 Relatively Low Air-filled Porosity. *Soil Science Society of America Journal*, 48(1), 3–6.
555 <https://doi.org/10.2136/sssaj1984.03615995004800010001x>
- 556 Shao, J., Zhou, X., Luo, Y., Li, B., Aurela, M., Billesbach, D., Blanken, P. D., Bracho, R.,
557 Chen, J., Fischer, M., Fu, Y., Gu, L., Han, S., He, Y., Kolb, T., Li, Y., Nagy, Z., Niu, S.,
558 Oechel, W. C., ... Zhang, J. (2015). Biotic and climatic controls on interannual variability
559 in carbon fluxes across terrestrial ecosystems. *Agricultural and Forest Meteorology*, 205,
560 11–22. <https://doi.org/10.1016/j.agrformet.2015.02.007>
- 561 Shao, P., Zeng, X., Moore, D. J. P., & Zeng, X. (2013). Soil microbial respiration from
562 observations and Earth System Models. *Environmental Research Letters*, 8(3), 034034.
563 <https://doi.org/10.1088/1748-9326/8/3/034034>
- 564 Sihi, D., Gerber, S., Inglett, P. W., & Inglett, K. S. (2016). Comparing models of microbial–
565 substrate interactions and their response to warming. *Biogeosciences*, 13(6), 1733–1752.
566 <https://doi.org/10.5194/bg-13-1733-2016>
- 567 Tang, J., Baldocchi, D. D., Qi, Y., & Xu, L. (2003). Assessing soil CO₂ efflux using continuous
568 measurements of CO₂ profiles in soils with small solid-state sensors. *Agricultural and Forest
569 Meteorology*, 15(1), 1–10. <https://doi.org/10.1016/j.agrformet.2003.07.001>

- 569 *Meteorology*, 118(3), 207–220. [https://doi.org/10.1016/S0168-1923\(03\)00112-6](https://doi.org/10.1016/S0168-1923(03)00112-6)
- 570 Tang, J., Misson, L., Gershenson, A., Cheng, W., & Goldstein, A. H. (2005). Continuous
571 measurements of soil respiration with and without roots in a ponderosa pine plantation
572 in the Sierra Nevada Mountains. *Agricultural and Forest Meteorology*, 132(3), 212–227.
573 <https://doi.org/10.1016/j.agrformet.2005.07.011>
- 574 Taylor, J. R. (2022). *An Introduction to Error Analysis: The Study of Uncertainties in Physical*
575 *Measurements, Third Edition* (3rd ed.). University Science Press.
- 576 Wilson, S. J., Bond-Lamberty, B., Noyce, G., Bittencourt Peixoto, R., & Megonigal, J. P.
577 (2024). Fluxfinder: An R Package for Reproducible Calculation and Initial Processing of
578 Greenhouse Gas Fluxes From Static Chamber Measurements. *Journal of Geophysical Re-*
579 *search: Biogeosciences*, 129(11), e2024JG008208. <https://doi.org/10.1029/2024JG008208>
- 580 Yan, Z., Bond-Lamberty, B., Todd-Brown, K. E., Bailey, V. L., Li, S., Liu, C., & Liu, C. (2018).
581 A moisture function of soil heterotrophic respiration that incorporates microscale processes.
582 *Nature Communications*, 9(1), 2562. <https://doi.org/10.1038/s41467-018-04971-6>
- 583 Yan, Z., Liu, C., Todd-Brown, K. E., Liu, Y., Bond-Lamberty, B., & Bailey, V. L. (2016).
584 Pore-scale investigation on the response of heterotrophic respiration to moisture conditions
585 in heterogeneous soils. *Biogeochemistry*, 131(1), 121–134. <https://doi.org/10.1007/s10533-016-0270-0>
- 587 Zhang, R., Kim, S., Kim, H., Fang, B., Sharma, A., & Lakshmi, V. (2023). Temporal
588 Gap-Filling of 12-Hourly SMAP Soil Moisture Over the CONUS Using Water Balance
589 Budgeting. *Water Resources Research*, 59(12), e2023WR034457. <https://doi.org/10.1029/2023WR034457>
- 591 Zhao, J. (2019). FluxCalR: A R package for calculating CO₂ and CH₄ fluxes from static
592 chambers. *Journal of Open Source Software*, 4(43), 1751. <https://doi.org/10.21105/joss.01751>
- 594 Zobitz, J., Ayres, E., O'Rourke, K., Werbin, Z., Lee, L., Abdi, R., Mehmeti, D., & Xiong, L.

595 (2024). *neonSoilFlux: Compute Soil Carbon Fluxes for the National Ecological Observatory*
596 *Network Sites.* <https://doi.org/10.32614/CRAN.package.neonSoilFlux>

597 Zobitz, J., & Zimmerman, N. (2025). *Supporting Code and Data for neonSoilFlux: An R*
598 *Package for Continuous Sensor-Based Estimation of Soil CO₂ Fluxes.* Zenodo. <https://doi.org/10.5281/zenodo.17516320>

599